Chemical Science

ROYAL SOCIETY OF CHEMISTRY

EDGE ARTICLE

View Article Online
View Journal | View Issue

Cite this: *Chem. Sci.*, 2025, **16**, 12397

All publication charges for this article have been paid for by the Royal Society of Chemistry

Received 20th April 2025
Accepted 3rd June 2025

DOI: 10.1039/d5sc02877a

rsc.li/chemical-science

An activatable unimolecular phototheranostic agent for synergistic chemo-photodynamic therapy†

Jinliang Han,[a] Kang Li,[a] Mingwang Yang,*[a] Jiangli Fan *[ab] and Xiaojun Peng [a]

Precise control over spatiotemporal release of cancer therapeutics remains a significant challenge in developing effective combination therapies. Herein, we report a hydrogen peroxide (H_2O_2)-activatable unimolecular platform (**ICy-Cb**) that integrates cancer imaging and synchronized dual-modal therapy. An iodized hemicyanine photosensitizer and chlorambucil are integrated into a single molecular structure that selectively reacts to the high concentration of H_2O_2 present in the tumor microenvironment. **ICy-Cb** initially exhibits no fluorescence and is therapeutically inert due to the suppression of its intramolecular charge transfer (ICT) effect. Upon exposure to tumor-associated H_2O_2, **ICy-Cb** simultaneously releases both therapeutic components, demonstrating exceptional tumor selectivity (5 to 8 folds higher activation in cancer cells), deep penetration in 3D tumor models (180 μm), and persistent tumor accumulation *in vivo*. Most importantly, this synchronized chemo-photodynamic agent achieves superior tumor growth inhibition (92%) compared to either monotherapy. This theranostic agent represents a significant advancement for precision cancer treatment by enabling spatiotemporally controlled combination therapy within the tumor microenvironment.

Introduction

Cancer is a global malignant disease caused by disorderly cellular division and mutational growth.[1,2] Among cancer treatment modalities, chemotherapy remains predominant due to its systemic effectiveness in targeting metastatic cancer cells throughout the body, proven track record against various malignancies (especially blood cancers).[3] However, traditional chemotherapy, which relies solely on anticancer drugs, faces limitations such as low specificity to tumor cells and undesirable side effects, often resulting in suboptimal therapeutic outcomes.[4,5] Recently, photodynamic therapy (PDT), which exhibits high spatiotemporal selectivity, minimal systemic side effects, and noninvasiveness, has emerged as a promising alternative approach in oncological treatment.[6,7] During PDT, the photosensitizer (PS) sensitizes oxygen under light irradiation to produce highly oxidative reactive oxygen species (ROS), which cause tumor cell apoptosis or necrosis.[8–12] Among various photosensitizers, hemicyanine dyes represent ideal candidates for phototheranostic applications due to their excellent properties, including NIR absorption/emission profiles ($\lambda_{max} \geq 680$ nm), large molar extinction coefficients, and modifiable photochemical sites that enable deep tissue penetration and effective singlet oxygen generation.[13–17] However, the hypoxic microenvironment within deeper tumor regions greatly diminishes the generation of ROS, leading to a reduction in the therapeutic effectiveness of PDT.[18] With the continuous evolution of cancer cells, the therapeutic efficacy of single-modality treatments for malignant tumors has become increasingly limited.[19] As a contrast, combined therapy can capitalize on the complementarity of various treatment methods to achieve synergistic advantages, ultimately optimizing the overall therapeutic outcome.[20–22] For instance, chemotherapy damages cellular structures and modifies the permeability of cell membranes, thereby facilitating the uptake of PS and concurrently enhancing the sensitivity of cancer cells to oxidative stress. Conversely, the ROS generated by PDT can disrupt both the drug efflux pump and the cellular defense mechanisms, thus increasing drug retention and mitigating drug resistance of cancer cells.[23–25] The combination of PDT and chemotherapy creates a synergistic effect, where chemotherapy intensifies the effectiveness of PDT, and PDT, in turn, boosts the results of chemotherapy.

However, conventional combined therapy often employs a "cocktail" approach, which leads to significant challenges including inconsistent biodistribution, heterogeneous metabolism profiles, asynchronous activation at target sites, and unpredictable pharmacokinetic interactions.[26–28] Additionally, most therapeutic agents are in an "always-on" state, resulting in

[a]State Key Laboratory of Fine Chemicals, Frontier Science Center for Smart Materials, Dalian University of Technology, Dalian, 116023, China. E-mail: yangmw66@126.com; fanjl@dlut.edu.cn

[b]Liaoning Binhai Laboratory, Dalian, 116023, China

† Electronic supplementary information (ESI) available. See DOI: https://doi.org/10.1039/d5sc02877a

a series of side effects such as high toxicity to normal cells, weak tumor specificity, and high phototoxicity, ultimately reducing their therapeutic efficacy against tumors.[13,29–31] In contrast, therapeutic agents capable of being activated by a specific biological target of interest display "off–on" characteristics, thereby significantly reduce side effects while improving both the biosafety and therapeutic efficacy.[32–35] Hydrogen peroxide (H_2O_2), as a critical reactive oxygen species substantially overexpressed in various tumor types with significantly higher concentrations in tumor cells (5 μM to 1.0 mM) compared to normal cells (less than 0.7 μM), provides an ideal biomarker for developing tumor-specific theranostic agents.[36–39] Ideal H_2O_2-responsive systems should possess three key attributes: specific activation by tumor microenvironment H_2O_2; simultaneous release of multiple therapeutic components for synergistic effects; and integration of both imaging and therapeutic capabilities for real-time monitoring of drug distribution and efficacy. However, most current H_2O_2-responsive systems achieve only single treatment modality or require complex nanocarriers, which increase the complexity of preparation and potentially introduce new safety concerns.

In this work, we present a novel H_2O_2-activatable unimolecular phototheranostic agent, **ICy-Cb**, for cancer visualization and synchronized combination therapy (Scheme 1). In the architecture of this designed system, both a photosensitizer and chemotherapeutic agent are strategically incorporated within a single molecular framework that specifically responds to elevated H_2O_2 levels in the tumor microenvironment. **ICy-Cb** is initially non-fluorescent and therapeutically inactive as its intramolecular charge transfer (ICT) is inhibited by the pinacol borate moiety that cages the hemicyanine dye. Only in the presence of tumor-associated H_2O_2, **ICy-Cb** undergoes site-specific oxidation and releases the iodized hemicyanine photosensitizer (**ICy-OH**) and chlorambucil (**Cb**) through self-immolative fragmentation, enabling PDT and chemotherapy respectively. **ICy-Cb** demonstrates remarkable selectivity, providing high-contrast differentiation between normal cells and multiple cancer cell lines (4T1, MCF-7, HeLa) with 5–8 folds higher activation in cancer cells. Three-dimensional tumor models revealed exceptional penetration capabilities (up to 180 μm depth), facilitating effective treatment throughout the tumor mass. *In vivo* imaging confirmed selective accumulation in tumor tissues with persistent fluorescence signals lasting 24 hours, enabling precise tumor visualization. Most significantly, when compared to single-modality approaches (chemotherapy or photodynamic therapy alone), **ICy-Cb**-mediated synchronized combination therapy demonstrated dramatically enhanced therapeutic efficacy, achieving remarkable tumor growth inhibition (92% *in vivo*). By integrating dual therapeutic modalities within a single H_2O_2-responsive molecular platform,

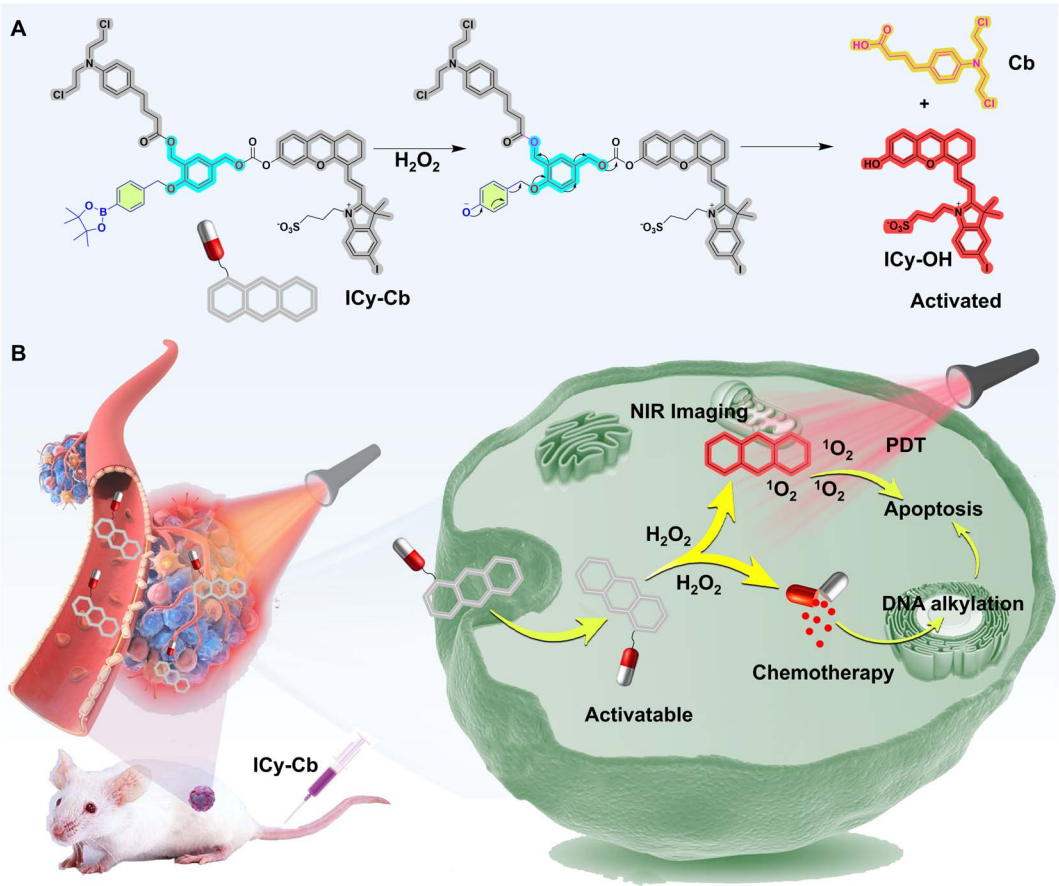

Scheme 1 Schematic diagram of (A) molecular structure and H_2O_2-activated (B) *in vivo* anti-tumor mechanism of **ICy-Cb**.

ICy-Cb addresses a fundamental challenge in cancer treatment: achieving precise spatiotemporal control over combination therapy while minimizing systemic toxicity, thereby representing a promising approach for translational applications in cancer theranostic.

Results and discussion

Design and synthesis of ICy-Cb

The strategic design and synthesis of **ICy-Cb** were accomplished following the synthetic route depicted in Schemes 1 and S1,† with the aim of creating a dual-modality theranostic agent. An iodized hemicyanine dye (**ICy-OH**) was integrated into the system as an activatable PS for PDT.[13] Chlorambucil (**Cb**), a clinically validated chemotherapeutic agent widely utilized in cancer treatment, exerts its primary pharmacological action by inducing cross-linking of the DNA double helix structure in cancer cells, thereby disrupting DNA replication and extension processes, ultimately resulting in cancer cell death and tumor suppression.[40–42] Notably, when the carboxyl moiety of butyric acid forms an ester bond with a hydroxyl group, the cytotoxicity of **Cb** is significantly attenuated due to inhibited oxidation at the β-position of the butyrate side chain, making it an ideal candidate for our prodrug system.[22] The rationally designed molecule (**ICy-Cb**) was engineered to undergo activation specifically by elevated levels of H_2O_2 in the tumor microenvironment, facilitating the simultaneous release of both the PS and chemotherapeutic agent for concurrent PDT and chemotherapy, respectively (Fig. 1A). To further validate this strategy, we synthesized a control molecule, **ICy**, by conjugating **ICy-OH** with pinacyl 4-phenylborate benzyl alcohol, which selectively releases the photosensitizer **ICy-OH** in the presence of H_2O_2 (Scheme S2†). All intermediates and final compounds (**ICy-Cb** and **ICy**) were thoroughly characterized *via* ^{1}H NMR, ^{13}C NMR, MS, and HRMS analyses (see ESI†), confirming their structural integrity and purity essential for subsequent biological evaluations.

Sensing property of probe ICy-Cb

Upon successful synthesis and characterization of the novel compound **ICy-Cb**, we thoroughly investigated its sensitivity and specificity toward H_2O_2. The absorption spectrum of **ICy-Cb**, illustrated in Fig. 1B, displays a prominent absorption peak centered at 600 nm, while exhibiting negligible fluorescence emission (Fig. 1C), indicating the effective quenching of fluorescence in its native state. Upon exposure to H_2O_2, a remarkable spectral transformation occurs: the absorption peak at 600 nm diminishes concurrently with the emergence of a new band at 670 nm (Fig. 1B), signaling the structural conversion of the molecule. Sequential addition of increasing H_2O_2 concentrations to the **ICy-Cb** solution resulted in progressive enhancement of the emission band at 720 nm (under 640 nm excitation), reaching maximum intensity after 60 minutes (Fig. 1C and E). Notably, the fluorescence intensity at 720 nm demonstrated a strong linear correlation with H_2O_2 concentration, yielding a calculated detection limit of 0.3 μM mL^{-1} (Fig. 1D). We postulate that the significant spectral shift observed can be attributed to the H_2O_2-mediated conversion of **ICy-Cb** to **ICy-OH** through a specific molecular mechanism. The activation process proceeds through several discrete sequential steps: initially, the pinacol borate moiety undergoes oxidation by H_2O_2 to form a hydroxyl intermediate. Subsequently, electronic rearrangement within this activated species triggers the cleavage of the benzyl C–O bonds *via* 4- or 6-electron reduction pathways, facilitating the simultaneous release of both **Cb** and **ICy-OH**. Concurrently, the cleaved intermediates react with water molecules to spontaneously generate *p*-hydroxybenzyl alcohol. This decapping process effectively restores ICT within the hemicyanine structure, thereby inducing pronounced fluorescence enhancement in the near-infrared region, which is highly advantageous for *in vivo* imaging applications. To validate our proposed mechanism with chemical precision, we conducted comprehensive analysis of the reaction products using Electrospray Ionization Mass Spectrometry (ESI-MS). As illustrated in Fig. S1,† the reaction mixture containing probe **ICy-Cb** and H_2O_2 revealed two distinctive mass peaks at m/z = 617.0711 and m/z = 304.0811, which correspond precisely to the theoretical molecular masses of the expected products **ICy-OH** ($[M]^+$ = 617.0733) and **Cb** ($[M + H]^+$ = 304.0866), providing direct evidence for our proposed reaction pathway and product formation.

For more rigorous confirmation, we employed High-Performance Liquid Chromatography (HPLC) analysis, which provided additional quantitative evidence for the simultaneous liberation of **ICy-OH** and **Cb**. Following a 2 hours reaction period with H_2O_2, the chromatographic peak associated with the parent probe **ICy-Cb** (retention time 17 min) was virtually eliminated (Fig. 1F). Concurrently, two new distinctive peaks emerged at retention times of 6.5 min and 4.5 min, aligning precisely with the retention times of authentic standards of **ICy-OH** and **Cb**, respectively (Fig. 1F). The H_2O_2-catalyzed cleavage kinetics of **ICy-Cb** were quantitatively monitored through time-course HPLC analysis. This investigation demonstrated the simultaneous accumulation of **Cb** and **ICy-OH** in a consistent 1 : 1 stoichiometric ratio, confirming their synchronized release during the oxidative process (Fig. 1G and H). The reaction reached equilibrium after 90 minutes, with calculated release efficiencies of 86.7% and 85.3% for **Cb** and **ICy-OH**, respectively. These findings conclusively demonstrate the efficient H_2O_2-mediated dissociation of **ICy-Cb** into its constituent therapeutic components, **Cb** and **ICy-OH**.

To ensure the clinical applicability of our probe, we conducted a comprehensive specificity analysis to evaluate the selectivity of **ICy-Cb** toward H_2O_2 among various potential biological interferents. The probe was incubated with a diverse array of biologically relevant reactive species including nitric oxide (NO), peroxynitrite (ONOO–), hydroxyl radical ($^{\bullet}$OH), singlet oxygen ($^1O_2$), superoxide (O^{2-}), peroxyl radical (ROO$^{\bullet}$), *tert*-butoxyl radical (t-BuO$^{\bullet}$), and hypochlorous acid (HClO). As demonstrated in Fig. 1I, upon excitation at 640 nm, only the **ICy-Cb** + H_2O_2 system exhibited significant fluorescence enhancement at 720 nm, while all other analytes induced negligible changes in fluorescence intensity, even after extended

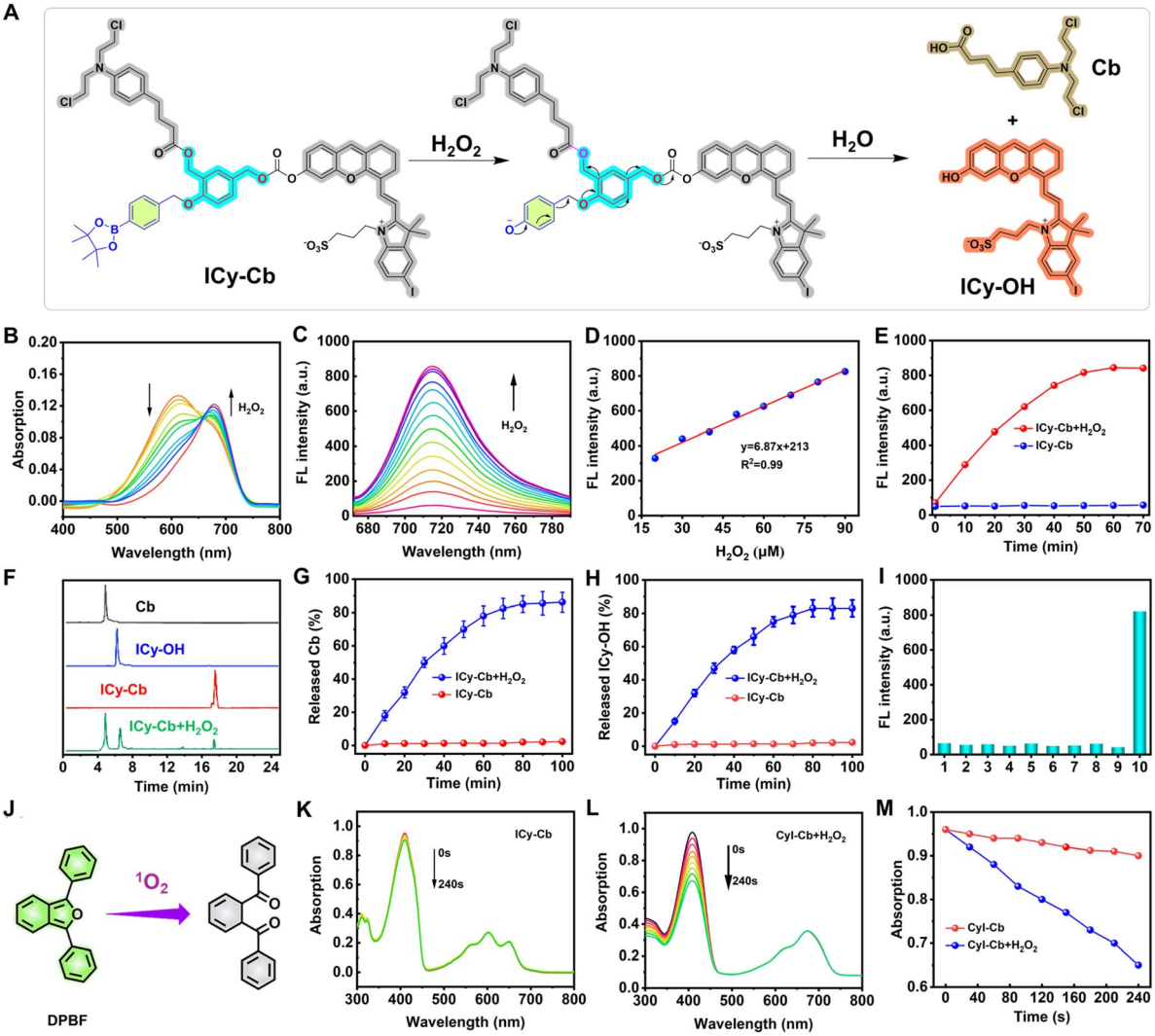

Fig. 1 (A) Schematic illustration of H_2O_2-mediated fluorescence turn-on and drug release of **ICy-Cb**. (B) UV-vis and (C) Fluorescence spectra absorbance changes of **ICy-Cb** (5 μM) in PBS buffer (10.0 mM, pH 7.4, containing 30% DMSO), after introduction of H_2O_2 (0.0–100.0 μM). (D) The linear relationship between $I_{720\ nm}$ and the concentration of H_2O_2 (20.0–90.0 μM). (E) Time-dependent fluorescence of **ICy-Cb** with the addition of H_2O_2 (100.0 μM) in PBS buffer (10.0 mM, pH 7.4, containing 30% DMSO). (F) HPLC chromatographic analysis was performed on several samples: pure **Cb** (black), **ICy-OH** (blue), **ICy-Cb** (red), and a mixture (green) of **ICy-Cb** and H_2O_2. Release efficiency of (G) **Cb** and (H) **ICy-OH** from **ICy-Cb**. (I) Fluorescence measurements of **ICy-Cb** (5.0 μM) were recorded in response to H_2O_2 (100.0 μM) and various other substances (100.0 μM): (1) Blank, (2) NO, (3) $ONOO^-$, (4) $^{\bullet}OH$, (5) $^1O_2$, (6) O_2^-, (7) $ROO^{\bullet}$, (8) *t*-$BuO^{\bullet}$, (9) HClO and (10) H_2O_2. All measurements were taken 90 minutes after adding the stimulants at room temperature, using an excitation wavelength of 670 nm and an emission wavelength of 720 nm. (J) Schematic illustration of DPBF detecting $^1O_2$. Photodegradation curves of DPBF in the presence of **ICy-Cb** (K) and **ICy-Cb** + H_2O_2 (L) were obtained under 660 nm light irradiation for varying durations (0–240 s). (M) DPBF degradation (monitored at 415 nm) induced by **ICy-Cb** and **ICy-OH** under irradiation 660 nm irradiation.

incubation periods of 90 minutes. These results unequivocally confirm the remarkable selectivity of **ICy-Cb** for H_2O_2 activation, a critical requirement for applications in complex biological systems.

To evaluate the ROS generation capacity of our compounds following H_2O_2 activation, we performed comprehensive photochemical analyses based on the promising observation that **ICy-Cb** released **ICy-OH** with restored fluorescence upon H_2O_2 treatment. When liberated **ICy-OH** absorbs irradiation, molecules are elevated to an excited singlet state, with a portion of this energy being emitted as fluorescence-valuable for tumor imaging and drug tracking applications. The remaining excited molecules undergo intersystem crossing (ISC) to reach the triplet state, subsequently transferring energy to molecular oxygen to generate singlet oxygen ($^1O_2$), thereby enabling PDT. The 1,3-diphenlisobenzofuran (DPBF), as a $^1O_2$ capturing agent (Fig. 1J), was used to study the $^1O_2$ generation capacity of **ICy-Cb**, **ICy-Cb** +H_2O_2 and **ICy-OH** by the absorption changes of DPBF at 415 nm. As seen in Fig. 1K–M, the absorbance of DPBF at 415 nm decreased dramatically in the presence of **ICy-Cb**+H_2O_2 under 660 nm (10 mW cm^{-2}) light irradiation with a degradation curve closely matching that of **ICy-OH** (Fig. S4†).

However, under the same conditions, no significant change in the absorption of DPBF in **ICy-Cb** solution can be observed (Fig. 1L). This is also illustrated by the data in Fig. 1M. These results indicate that **ICy-Cb** is an activatable PS whose PDT activity can be enhanced by H_2O_2. The singlet oxygen quantum yield ($\Phi\Delta$) was calculated to be 0.39% for **ICy-Cb** and 2.46% for **ICy-OH**, demonstrating that the H_2O_2-activated product **ICy-OH** displays significantly enhanced ROS production capacity (approximately 6.3-fold increase).

Subsequently, we examined the spectral characteristics of the control probe **ICy** in response to H_2O_2 (Fig. S2 and S3†). This probe displayed a primary absorption maximum at 605 nm with essentially no fluorescence emission at 720 nm in its native state. Upon exposure to H_2O_2, the probe exhibited a pronounced bathochromic shift in absorption to 670 nm, accompanied by significant enhancement of red fluorescence emission at 720 nm (λ_{ex} = 670 nm). This spectral behavior closely paralleled the fluorescence response pattern observed with probe **ICy-Cb**, further validating our molecular design rationale.

Fluorescence imaging of H_2O_2 in living cells

To assess the cellular applicability of **ICy-Cb** given its robust response to H_2O_2 and potent photodynamic properties, we conducted comprehensive cellular-level H_2O_2 imaging studies. Initially, we investigated the cellular uptake kinetics of **ICy-Cb** in 4T1 breast cancer cells. As illustrated in Fig. S5 and S6,† **ICy-Cb** exhibited detectable fluorescence within 40 minutes of incubation, with signal intensity progressively increasing over time, demonstrating efficient internalization and activation within cancer cells. To evaluate the probe's H_2O_2-responsive imaging capabilities, 4T1 cells loaded with **ICy-Cb** were subjected to various experimental conditions (Fig. 2A and B). In the control group (Fig. 2A), cells treated solely with **ICy-Cb** exhibited weak fluorescence. However, following treatment with lipopolysaccharide (LPS), which stimulates endogenous H_2O_2 production,[43] a significant enhancement in fluorescence intensity was observed. Similarly, direct addition of H_2O_2 resulted in significant fluorescence amplification. Confirmatory negative control experiments employing *N*-acetyl-cysteine (NAC),[44] a well-established reactive oxygen species scavenger, verified that the observed fluorescence modulation was specifically attributable to intracellular H_2O_2 levels.

To further investigate the subcellular organelle localization, various commercial trackers, including ER-Tracker Green, Mito-Tracker Green, Lyso-Tracker Green and DiO, as well as **ICy-Cb** (10 μM), were applied to 4T1 cells for 60 min respectively (Fig. S7†). The distribution of **ICy-Cb** in 4T1 overlaps most with ER-Tracker Green, with a correlation coefficient of 0.89. In contrast, the correlation coefficients between **ICy-Cb** and Mito Tracker Green, Lyso-Tracker Green or DiO were found to be 0.75, 0.55 and 0.27 respectively (Fig. S7†). Therefore, this molecule is primarily located in the endoplasmic reticulum.

Having characterized the cellular uptake and localization properties, we proceeded to evaluate **ICy-Cb**'s ability to simultaneously detect differential H_2O_2 levels across various cell types. We performed comparative imaging studies on normal ovarian epithelial cells (IOSE80) and multiple cancer cell lines: 4T1 (breast cancer), MCF-7 (breast cancer), and HeLa (cervical cancer). As shown in Fig. 2C, under identical imaging conditions with 10 μM **ICy-Cb**, tumor cells exhibited significantly brighter fluorescence compared to normal cells, with quantitative analysis revealing 5–8 folds higher fluorescence intensity in cancer cells (Fig. 2D). Flow cytometry analysis (Fig. 2E) independently confirmed these observations, providing quantitative single-cell resolution data that corroborated the microscopy findings. These results clearly indicate that cancer cells maintain higher basal H_2O_2 levels than normal cells, consistent with previous studies on cancer redox dysregulation. The ability of **ICy-Cb** to discriminate between normal and cancer cells based on their inherent H_2O_2 levels demonstrates its potential utility as a cancer-specific imaging agent for diagnostic applications.

In vitro cytotoxicity evaluation

To assess the therapeutic potential of our H_2O_2-activatable system, we first investigated whether activated **ICy-Cb** could effectively generate ROS within living cells, a prerequisite for photodynamic therapy efficacy. We employed 2′,7′-dichlorofluorescin diacetate (DCFH-DA) as an indicator of intracellular ROS. DCFH-DA itself is non-fluorescent; however, upon cellular internalization, it undergoes hydrolysis by intracellular esterases. The resulting compound can then be oxidized by ROS to produce 2,7-dichlorofluorescein (DCF), which exhibits strong fluorescence emission. Our experimental results, as illustrated in Fig. 3B, demonstrated negligible fluorescence in cells treated with **ICy-Cb** in the absence of light stimulation. In contrast, when these pre-treated cells were subjected to red-light irradiation (660 nm), a significant enhancement in fluorescence intensity was observed (Fig. 3B). These findings provide compelling evidence that **ICy-Cb** functions as an H_2O_2-responsive, activatable PS capable of generating singlet oxygen upon activation, thus demonstrating its potential utility for PDT.

To further validate the intracellular singlet oxygen generation capability of our system, we employed Singlet Oxygen Sensor Green (SOSG) as a specific probe for detecting $^1O_2$ in living cells. As shown in Fig. S8,† 4T1 cells were initially incubated with **ICy-Cb** (10 μM) for 60 minutes, followed by treatment with SOSG (5 μM) for an additional 30 minutes. Upon irradiation with 660 nm light (10 mW cm^{-2}) for 10 minutes, a significant enhancement in green fluorescence (λ_{ex} = 488 nm, λ_{em} = 500–580 nm) was observed within the **ICy-Cb**-loaded cells. In contrast, control experiments conducted with **ICy-Cb** without light exposure exhibited minimal SOSG fluorescence, demonstrating that singlet oxygen generation is specifically triggered by light activation of the **ICy-Cb** system after its H_2O_2-mediated conversion to **ICy-OH**. These results provide direct evidence for the intracellular production of singlet oxygen during the photodynamic therapy process, further confirming the mechanistic basis of our dual-modality therapeutic approach.

Having confirmed the ROS-generating capability of our system, we proceeded to systematically evaluate the cytotoxicity

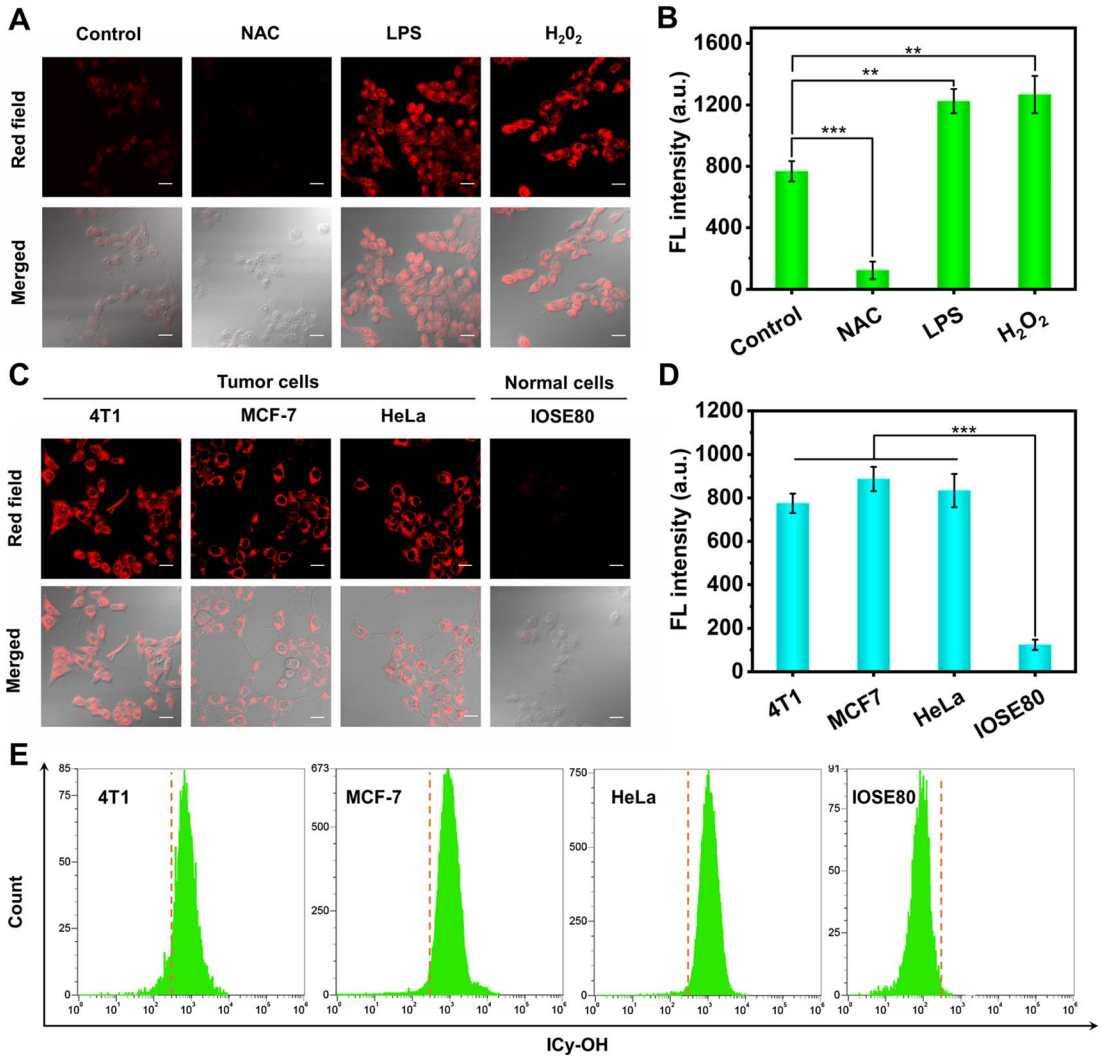

Fig. 2 (A) 4T1 cells pretreated with NAC (500 μM), LPS (1 μg mL^{-1}) and H_2O_2 (100 μM) for 30 min, then incubated with 10 μM **ICy-Cb** for 60 min. (λ_{ex} = 640 nm, λ_{em} = 670–750 nm) (B) Relative fluorescence intensity from (A). (C) Fluorescence images of tumor cells (4T1, MCF-7, HeLa) and normal cells (IOSE80) incubated with **ICy-Cb** (10 μM), respectively. (D) Relative fluorescence intensity from (C). (E) Data of flow cytometry after cells (4T1, MCF-7, HeLa and IOSE80) were stained by 10 μM **ICy-Cb** for 60 min. Scale bar = 10 μm.

profiles of various treatment regimens involving **ICy-Cb** using the 3-(4,5-dimethylthiazol-2-yl)-2,5-diphenyl tetrazolium bromide (MTT) assay, a gold standard for cell viability assessment. Initial assessment of the cytotoxicity on normal ovarian epithelial cells (IOSE80) revealed that **ICy-Cb** exhibited minimal toxicity, maintaining approximately 87% cell viability following 24 hours incubation at concentrations up to 10 μM, regardless of light exposure conditions (Fig. S10†). This favorable safety profile in normal cells substantiates the selective therapeutic potential of our designed probe, a critical consideration for clinical translation.

Additionally, we evaluated the cytotoxicity profiles across multiple cancer cell lines-4T1, MCF-7, and HeLa-incubated with varying concentrations of **ICy-Cb**. For comparative analysis, **ICy** and commercial **Cb** were examined under identical experimental conditions (Fig. 3A). As evidenced in Fig. 3C–F, **ICy** exhibited negligible cytotoxicity toward cancer cells under dark conditions. Notably, **Cb**, despite its status as a first-line clinical chemotherapeutic agent, demonstrated suboptimal cytotoxicity against these cancer cell lines at the tested dosage and treatment frequency. Similarly, **ICy-Cb** displayed limited cytotoxicity under dark conditions, primarily attributable to the released **Cb**, as evidenced by cellular viability trends that paralleled those observed in the **Cb** treatment group. Under light irradiation conditions, **ICy** demonstrated significant cytotoxicity, attributable to the release of **ICy-OH** that facilitates effective PDT-mediated cell killing. Most notably, we observed markedly enhanced cell death when cells were treated with **ICy-Cb** followed by light irradiation (Fig. 3C–F). This augmented cytotoxic effect results from the simultaneous action of **ICy-OH**-mediated phototoxicity and **Cb**-induced chemotherapeutic effects, effectively achieving the intended dual-modality therapeutic approach. This synergistic effect highlights the significant advantage of our rationally designed H_2O_2-activatable

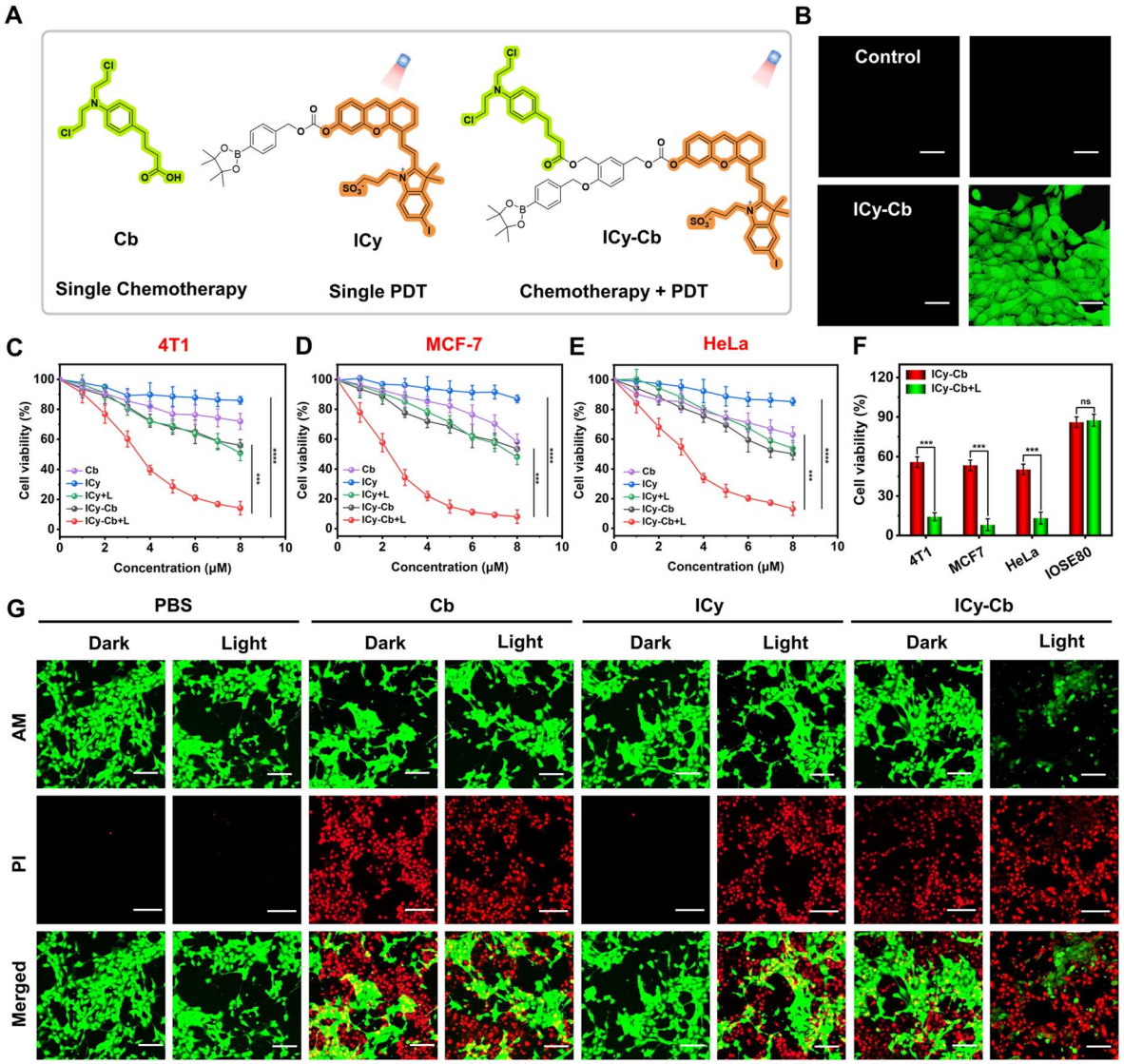

Fig. 3 (A) Chemical structure formula of **Cb** (single Chemotherapy), **ICy** (single PDT) and **ICy-Cb** (chemotherapy + PDT). (B) Evaluation of ROS generation in 4T1 cells. Scale bars: 20 μm. Evaluation of the cytotoxicity of **ICy-Cb** on (C) 4T1 cells, (D) MCF-7 cells and (E) HeLa cells at various doses under dark or light, NIR light (660 nm, 10 mW cm^{-2}, 20 min). (F) Cytotoxicity of **ICy-Cb** (6.0 μM) to different cell lines after different treatments. $N = 5$. (G) AM/PI fluorescent imaging for distinguishing living and dead cells. Scale bars represent 200 μm, (*t* tests, $n = 5$, mean ± SD, $^{*}p < 0.05$, $^{**}p < 0.01$, $^{***}p < 0.001$, $^{****}p < 0.0001$).

theranostic agent compared to either monotherapy approach, demonstrating superior therapeutic efficacy through the combination of photodynamic and chemotherapeutic modalities.

To visually confirm our cytotoxicity findings, we conducted additional investigations using dual fluorescent staining with calcein acetoxymethyl ester (calcein-AM) and propidium iodide (PI). Calcein-AM generates green fluorescence exclusively in viable cells, while PI produces red fluorescence when intercalated with nucleic acids in dead cells. As depicted in Fig. 3G, these visual results corroborated our quantitative MTT data: the cytotoxic efficacy of **ICy-Cb** under dark conditions was limited and comparable to that of **Cb** alone. However, following light exposure, cells throughout the entire microscopic field exhibited prominent red fluorescent signals, indicating widespread cell death induced by activated **ICy-Cb**. This fluorescence-based visualization provides compelling evidence for the potent therapeutic efficacy of our H_2O_2-activatable dual-modality system when both the photosensitizer and chemotherapeutic components are simultaneously activated.

Penetration and toxicity testing of probe on 3D-tumor spheres

To bridge the gap between two-dimensional cell culture findings and *in vivo* applications, we constructed 4T1-derived multicellular spheroids (MCSs) to systematically investigate the tumor penetration capabilities and H_2O_2-catalytic activity of **ICy-Cb** under conditions that better mimic the complexity of solid tumors. A key challenge in cancer therapy is achieving

sufficient penetration of therapeutic agents throughout the tumor mass. To evaluate this critical parameter, we performed *z*-axis scanning confocal microscopy of tumor spheroids after incubation with **ICy-Cb** (10 μM, 4 hours). As demonstrated in Fig. 4A and B, sequential scanning images along the *z*-axis (methodology illustrated in Fig. 4A) revealed that **ICy-Cb** exhibited exceptional penetration capability. Remarkably, substantial fluorescence intensity was detected even at depths of 180 μm within the spheroids (Fig. 4B), indicating activation of the probe throughout the tumor mass. This deep penetration capability is particularly significant as it addresses one of the major limitations of conventional photodynamic therapy and chemotherapeutic approaches.

Having established the penetration characteristics, we proceeded to evaluate the therapeutic efficacy of our dual-modality system in these 3D tumor models. Consistent with our two-dimensional cell culture findings, the vast majority of cells within tumor spheroids treated with **ICy** under dark conditions remained viable (Fig. 4C). Spheroids exposed to **Cb** exhibited limited cytotoxicity, indicating that at equivalent dosages, **Cb** demonstrates restricted therapeutic efficacy, similar to that observed with **ICy-Cb** under dark conditions. These observations in three-dimensional tumor models were consistent with our previous two-dimensional cell culture findings. Furthermore, **ICy**-treated spheroids exhibited partial cytotoxicity when exposed to light irradiation. In contrast, **ICy-Cb** treatment followed by light exposure resulted in nearly complete cell death throughout the spheroid structure (Fig. 4C). These results maintain the same efficacy trend observed in our previous MTT experiments. Through three-dimensional surface analysis of the fluorescence images (Fig. 4D), we confirmed our hypothesis regarding the enhanced penetration and therapeutic efficacy of our dual-modality system in three-dimensional tumor models.

To quantitatively evaluate the therapeutic efficacy in our 3D tumor model, we performed CellTiter-Glo@3D (CTG-3D) assays on spheroids following various treatment regimens. This ATP-based viability assay provides direct quantification of metabolically active cells within the 3D structures. As shown in Fig. S9,† treatment with **ICy-Cb** followed by light irradiation (660 nm, 10 mW cm^{-2}) resulted in the most significant reduction in luminescence intensity, indicating substantial decrease in viable cells compared to all other treatment groups. Moderate

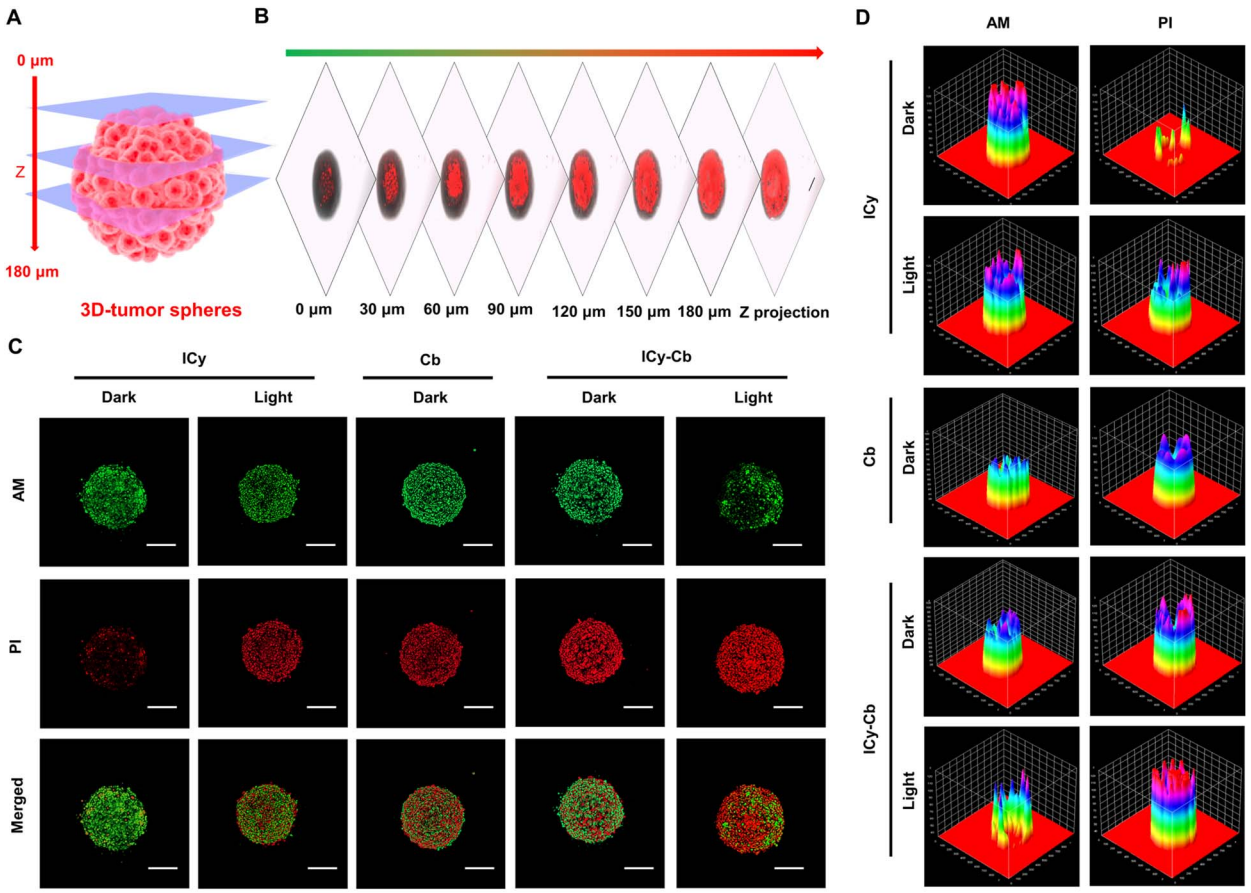

Fig. 4 (A) Diagrammatic illustration showing the z-slice scanning methodology used for cellular sphere analysis. (B) *Z*-axis fluorescence imaging series of tumor spheroids following **ICy-Cb** treatment. The Z-projection represents the composite overlay of all sequential images in the column. Scale bar represents 150 μm. (C) Visualization of spheroids using calcium-AM/PI dual staining protocol after various experimental treatments. Scale bar indicates 150 μm. (D) Three-dimensional surface plots depicting fluorescence intensity distribution throughout the spheroids along the *z*-axis.

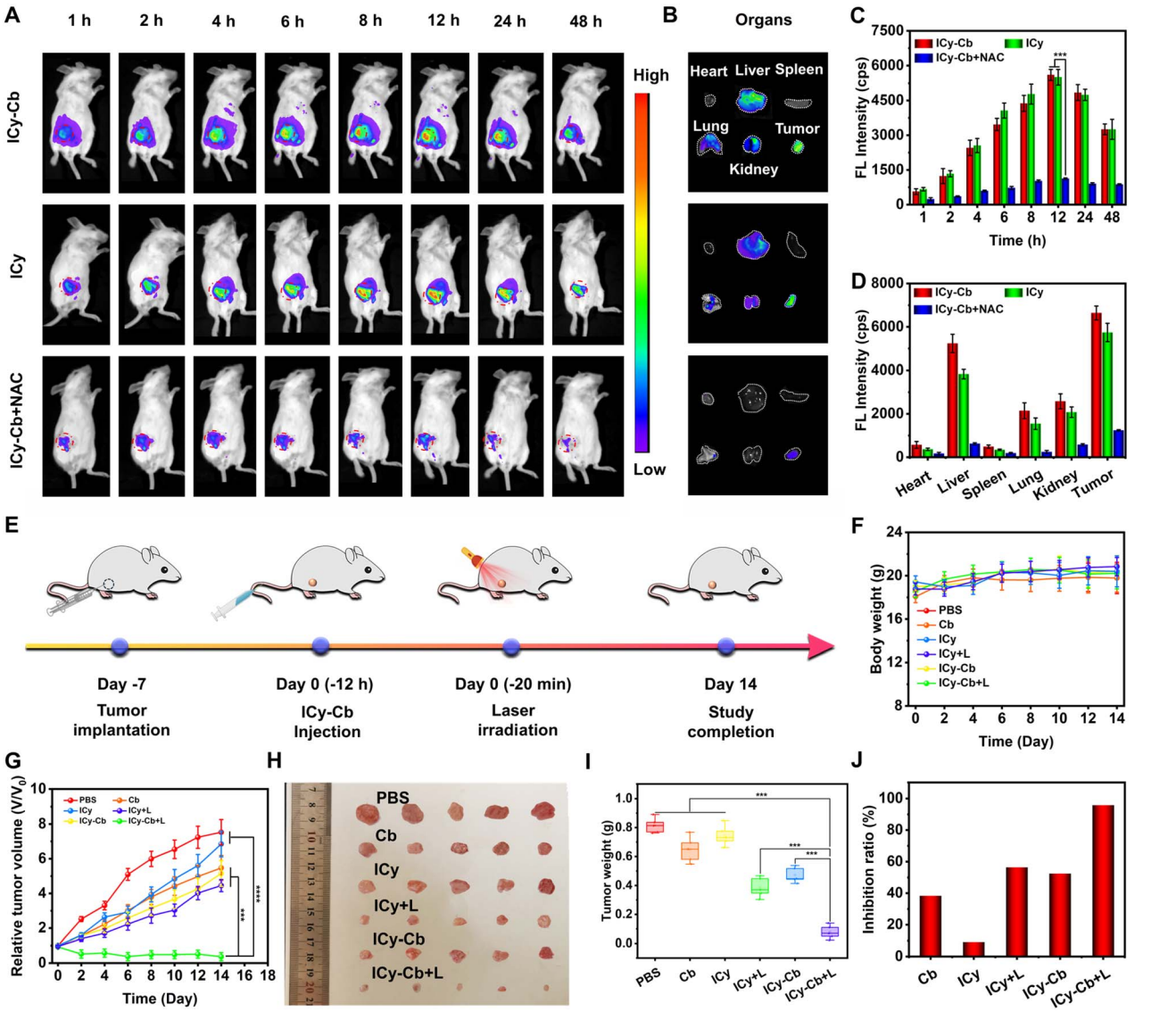

Fig. 5 (A) *In vivo* fluorescence visualization of tumor-bearing mice following various treatment protocols, imaged using 660 nm excitation wavelength and 680–720 nm emission collection. The tumor location is indicated by red circular marking. (B) *Ex vivo* fluorescence analysis of excised tumors and major organs at 48 hours post-intravenous administration of **ICy-Cb**, **ICy**, or **ICy-Cb** + NAC combination. (C) Temporal evolution of tumor-associated fluorescence signal intensity. (D) Quantitative analysis of mean fluorescence intensity corresponding to Fig. 5B. (E) Experimental timeline for tumor suppression studies using **ICy-Cb**-based interventions. (F) Body weight fluctuations across different treatment groups throughout the study period. (G) Comparative tumor volume progression across treatment cohorts (values presented as mean ± SD, $n = 5$). (H) Representative photographs of excised tumors from each experimental group following treatment completion. (I) Terminal tumor weight measurements across treatment groups. (J) Tumor growth inhibition efficacy comparison between different therapeutic interventions (statistical analysis: *t* tests, $n = 5$, data shown as mean ± SD, significance levels: $^{*}p < 0.05$, $^{**}p < 0.01$, $^{***}p < 0.001$, $^{****}p < 0.0001$).

reductions in viability were observed in spheroids treated with either ICy plus light (PDT only) or **ICy-Cb** without light (chemotherapy only), while Cb alone exhibited limited efficacy. These quantitative data strongly align with our qualitative observations from the Calcein-AM/PI imaging, confirming that the combination of photodynamic and chemotherapeutic modalities provides superior efficacy against 3D tumor models compared to either treatment alone. The enhanced performance in these structurally complex spheroids, which better mimic solid tumors than monolayer cultures, further supports the potential translational value of our dual-modal system.

In vivo antitumor therapy

Based on the promising *in vitro* results, we investigated the potential of **ICy-Cb** as a tumor-targeted prodrug *in vivo*. We established 4T1-bearing BALB/c mouse models for these experiments. Following tail vein injection of either **ICy-Cb** or **ICy**, we monitored activation and biodistribution using an *in vivo* imaging system (IVIS). As a negative control, NAC was administered *para*-tumorally to inhibit H_2O_2. As shown in Fig. 5A and C, minimal fluorescence signals were detected during the first 2 hours post-injection of **ICy-Cb**. However,

fluorescence intensity at tumor sites progressively increased over time, with substantial signals still present at 24 hours. Mice receiving **ICy** demonstrated comparable fluorescence activation patterns. Conversely, tumors pre-treated with NAC showed significantly reduced fluorescence throughout the observation period (Fig. 5A and C), confirming the compounds' selective activation in high-ROS tumor environments. At the 48 hours timepoint, mice were euthanized for *ex vivo* imaging of tumors and major organs, revealing that most activated **ICy-Cb** or **ICy** remained localized at tumor sites, with metabolic clearance occurring through hepatic and renal pathways (Fig. 5B and D). NAC-pretreated mice displayed lower overall signal intensity due to reduced **ICy-Cb** activation.

Having confirmed tumor-targeting capabilities, we evaluated therapeutic efficacy in tumor-bearing mice (Fig. 5E). Seven days after subcutaneous 4T1 cell implantation, mice with comparable tumor volumes were randomly assigned to six treatment groups ($n = 5$): (1) PBS (control), (2) **Cb** (chemotherapy), (3) **ICy** alone, (4) **ICy** + NIR light (PDT only), (5) **ICy-Cb** (chemotherapy only), and (6) **ICy-Cb** + NIR light (combination therapy). For light-treated groups, tumors were irradiated with 660 nm light (50 mW cm^{-2}, 20 min) 12 hours post-injection. Throughout the 14 days treatment period, body weight and tumor dimensions were recorded every other day. Results shown in Fig. 5F–I revealed no significant weight loss across all treatment groups, indicating minimal acute toxicity of **ICy-Cb** (Fig. 5F). Tumor growth curves (Fig. 5G) demonstrated rapid tumor progression in the PBS control group. The clinical agent **Cb** showed limited tumor inhibition at the administered dose and frequency. While **ICy** alone had negligible impact on tumor growth, **ICy-Cb** without light activation produced modest tumor growth delay, attributed to the chemotherapeutic effect of **Cb** released following H_2O_2 activation (Fig. 5G–I). The **ICy** plus light group exhibited significant tumor inhibition (TGI = 57%) due to the photodynamic effect of released **ICy-OH** within the tumor microenvironment. Most notably, mice receiving **ICy-Cb** with light exposure demonstrated superior tumor growth inhibition, achieving a 92% inhibition rate compared to either monotherapy approach (Fig. 5J). This enhanced therapeutic outcome can be attributed to the synergistic effects of combined chemotherapy and photodynamic therapy. After a 14 days treatment period, the mice were humanely euthanized and the tumors were surgically excised. Subsequently, tumor weights were measured and photographic evidence was obtained to further validate the observed growth patterns (Fig. 5H and I). These organs were then processed into paraffin sections and subjected to hematoxylin and eosin (H&E) staining. As illustrated in Fig. S11,† no discernible differences were observed in the organs of the PDT group compared to those treated with PBS. Moreover, examination revealed no abnormalities in physiological morphology or histopathological lesions, suggesting minimal toxicity of **ICy-Cb** to normal tissues. The comprehensive findings validate **ICy-Cb** as a highly efficient and activatable chemo-photodynamic agent, thereby demonstrating its significant potential for both tumor imaging and growth inhibition.

Conclusions

In conclusion, this study introduces a H_2O_2-responsive unimolecular phototheranostic agent, **ICy-Cb**, that strategically integrates cancer imaging and synchronized dual-modal therapy. In the structure of this engineered system, both a photosensitizer and a chemotherapeutic drug are integrated into a single molecular design that selectively reacts to the high levels of H_2O_2 present in the tumor microenvironment. The molecule effectively transitions from inactive to active states upon H_2O_2 exposure, simultaneously releasing both therapeutic components while generating near-infrared fluorescence for real-time visualization. **ICy-Cb** demonstrated exceptional tumor selectivity with 5 to 8 folds higher activation in cancer cells, deep tissue penetration (180 μm) in 3D tumor models, and sustained tumor accumulation *in vivo*. The synergistic effect of combined chemo-photodynamic therapy resulted in remarkable tumor growth inhibition (92%), substantially outperforming either monotherapy. Importantly, minimal toxicity to normal tissues was observed throughout treatment. Collectively, **ICy-Cb** represents a significant advancement in precision cancer theranostics by enabling spatiotemporally controlled combination therapy while minimizing systemic toxicity.

Ethical statement

All procedures involving animals adhered to the guidelines outlined in the Guide for the Care and Use of Laboratory Animals issued by the National Institutes of Health. The research protocol received approval from the Animal Ethics Committee at Dalian University of Technology (protocol number: 2018-043).

Data availability

The data that support the findings of this study are available in the ESI† of this article.

Author contributions

J. H. and J. F. conceived and designed the experiments for this project. J. H. performed the synthetic work and carried out the characterization of the compounds. J. H. and K. L. contributed to the photophysical experiments. J. H. and M. Y. conducted data analysis and prepared the initial manuscript, with all other authors contributing to revisions. X. P. supervised the work. All authors discussed the results and provided feedback on the manuscript.

Conflicts of interest

The authors declare no competing financial interests.

Acknowledgements

This work was financially supported by the National Natural Science Foundation of China (21925802, 22338005, 22308049),

Liaoning Binhai Laboratory (LBLB-2023-03), the Fundamental Research Funds for the Central Universities (DUT22LAB601).

Notes and references

1 R. L. Siegel, K. D. Miller, H. E. Fuchs and A. Jemal, *Ca-Cancer J. Clin.*, 2021, **71**, 7.
2 D. Huang, J. Yin, Y. Zou, H. Huang, S. Long, W. Sun, J. Du, J. Fan and X. Peng, *Smart Mol.*, 2024, **2**, e20240005.
3 B. Sun, C. Luo, W. Cui, J. Sun and Z. He, *J. Controlled Release*, 2017, **264**, 145.
4 B. A. Chabner and T. G. Roberts, *Nat. Rev. Cancer*, 2005, **5**, 65.
5 M. Deng, P. Wang, Z. Zhai, Y. Liu, D. Cheng, L. He and S. Li, *Anal. Chem.*, 2025, **97**, 2998.
6 X. Li, S. Lee and J. Yoon, *Chem. Soc. Rev.*, 2018, **47**, 1174.
7 B. M. Luby, C. D. Walsh and G. Zheng, *Angew. Chem., Int. Ed.*, 2019, **58**, 2558.
8 J. Wan, L. Ren, X. Li, S. He, Y. Fu, P. Xu, F. Meng, S. Xian, K. Pu and H. Wang, *Proc. Natl. Acad. Sci. U. S. A.*, 2023, **120**, e2210385120.
9 R. An, X. Cheng, S. Wei, Y. Hu, Y. Sun, Z. Huang, H.-Y. Chen and D. Ye, *Angew. Chem., Int. Ed.*, 2020, **59**, 20636.
10 Y. Bu, T. Xu, X. Zhu, J. Zhang, L. Wang, Z. Yu, J. Yu, A. Wang, Y. Tian, H. Zhou and Y. Xie, *Chem. Sci.*, 2020, **11**, 10279.
11 X. Yang, D. Wang, J. Zhu, L. Xue, C. Ou, W. Wang, M. Lu, X. Song and X. Dong, *Chem. Sci.*, 2019, **10**, 3779.
12 Y. Peng, R. Mo, M. Yang, H. Xie, F. Ma, Z. Ding, S. Wu, J. W. Y. Lam, J. Du, J. Zhang, Z. Zhao and B. Z. Tang, *ACS Nano*, 2024, **18**, 26140.
13 F. Xu, H. Li, Q. Yao, H. Ge, J. Fan, W. Sun, J. Wang and X. Peng, *Chem. Sci.*, 2019, **10**, 10586.
14 H. Zhang, C. Shi, F. Han, L. Cai, H. Ma, S. Long, W. Sun, J. Du, J. Fan, X. Peng and X. Chen, *Biomaterials*, 2023, **302**, 122365.
15 J. Yuan, H. Yang, W. Huang, S. Liu, H. Zhang, X. Zhang and X. Peng, *Chem. Soc. Rev.*, 2025, **54**, 341.
16 C. Zhao, W. Sun, Y. Zhu, X. Huang, Y. Sun, H.-Y. Wang, Y. Pan and Y. Liu, *J. Med. Chem.*, 2024, **67**, 22322.
17 Z. Cheng, S. Benson, L. Mendive-Tapia, E. Nestoros, C. Lochenie, D. Seah, K. Y. Chang, Y. Feng and M. Vendrell, *Angew. Chem., Int. Ed.*, 2024, **63**, e202404587.
18 N. Kurt Yilmaz and C. A. Schiffer, *Chem. Rev.*, 2021, **121**, 3235.
19 Y. You, H. Liu, J. Zhu, Y. Wang, F. Pu, J. Ren and X. Qu, *Chem. Sci.*, 2022, **13**, 7829.
20 Y. Yang, Y. Zhang, R. Wang, X. Rong, T. Liu, X. Xia, J. Fan, W. Sun and X. Peng, *Chin. Chem. Lett.*, 2022, **33**, 4583.
21 J. Han, M. Yang, K. Li, W. Liu, J. Fan and X. Peng, *Small*, 2025, **21**, 2410925.
22 Y. Zou, D. Huang, S. He, X. Song, W. Liu, W. Sun, J. Du, J. Fan and X. Peng, *Chem. Sci.*, 2023, **14**, 1010.
23 S. Diao, Y. Liu, Z. Guo, Z. Xu, J. Shen, W. Zhou, C. Xie and Q. Fan, *Adv. Healthcare Mater.*, 2023, **12**, 2301732.
24 H. Lou, L. Chu, W. Zhou, J. Dou, X. Teng, W. Tan and B. Zhou, *J. Mater. Chem. B*, 2022, **10**, 7955.
25 Z. Meng, F. Wei, R. Wang, M. Xia, Z. Chen, H. Wang and M. Zhu, *Adv. Mater.*, 2016, **28**, 245.
26 M. Wang, F. Zhang, C.-Q. Wang, N. Yin, Y. Wang, G. Qin, Q. Xu, J. Gong, H. Liu and X. Duan, *Anal. Chem.*, 2022, **94**, 5962.
27 R. Kumar, J. Han, H.-J. Lim, W. X. Ren, J.-Y. Lim, J.-H. Kim and J. S. Kim, *J. Am. Chem. Soc.*, 2014, **136**, 17836.
28 J. Fu, J. Han, T. Meng, J. Hu and J. Yin, *Chem. Commun.*, 2019, **55**, 12904.
29 X.-Z. Yang, S. Yao, J. Wu, J. Diao, W. He, Z. Guo and Y. Chen, *Smart Mol.*, 2024, **2**, e20240040.
30 J. F. R. Kerr, C. M. Winterford and B. V. Harmon, *Cancer*, 1994, **73**, 2013.
31 R. Wang, M. He, Z. Zhang, T. Qiu, Y. Xi, X. Zeng, J. Fan, W. Sun and X. Peng, *Smart Mol.*, 2024, **2**, e20240010.
32 A. G. Cheetham, R. W. Chakroun, W. Ma and H. Cui, *Chem. Soc. Rev.*, 2017, **46**, 6638.
33 M. H. Lee, A. Sharma, M. J. Chang, J. Lee, S. Son, J. L. Sessler, C. Kang and J. S. Kim, *Chem. Soc. Rev.*, 2018, **47**, 28.
34 X. Dong, R. K. Brahma, C. Fang and S. Q. Yao, *Chem. Sci.*, 2022, **13**, 4239.
35 Y. Yuan, R. T. K. Kwok, B. Z. Tang and B. Liu, *J. Am. Chem. Soc.*, 2014, **136**, 2546.
36 P. Huang, D. Wang, Y. Su, W. Huang, Y. Zhou, D. Cui, X. Zhu and D. Yan, *J. Am. Chem. Soc.*, 2014, **136**, 11748.
37 X. Meng, J. Zhang, Z. Sun, L. Zhou, G. Deng, S. Li, W. Li, P. Gong and L. Cai, *Theranostics*, 2018, **8**, 6025.
38 C. Yan, Z. Guo, Y. Shen, Y. Chen, H. Tian and W.-H. Zhu, *Chem. Sci.*, 2018, **9**, 4959.
39 S. Ye, J. J. Hu, Q. A. Zhao and D. Yang, *Chem. Sci.*, 2020, **11**, 11989.
40 R. K. Singh, S. Kumar, D. N. Prasad and T. R. Bhardwaj, *Eur. J. Med. Chem.*, 2018, **151**, 401.
41 A.-M. Chiorcea-Paquim and A. M. Oliveira-Brett, *J. Pharm. Biomed. Anal.*, 2023, **222**, 115036.
42 D. Fu, J. A. Calvo and L. D. Samson, *Nat. Rev. Cancer*, 2012, **12**, 104.
43 X. Luo, S. Cheng, W. Zhang, K. Dou, R. Wang and F. Yu, *ACS Sens.*, 2024, **9**, 810.
44 S. Chen, S. Li, H. Chen, Y. Gong, D. Yang, Y. Zhang and Q. Liu, *Sci. Adv.*, 2023, **9**, eadh4054.